Dynamic surface phases controlling asymmetry of high-rate lithiation and delithiation in phase-separating electrodes

Bonho Koo[1,7], Jinkyu Chung[1,7], Juwon Kim[1,7], Dimitrios Fraggedakis[2], Sungjae Seo[1], Chihyun Nam[1], Danwon Lee[1], Jeongwoo Han[1], Sugeun Jo[1], Hongbo Zhao[2], Neel Nadkarni[2], Jian Wang[3], Namdong Kim[4], Markus Weigand[5], Martin Z. Bazant[2,6,8], Jongwoo Lim[1,8]

[1]*Department of Chemistry, Seoul National University, Seoul 08826, South Korea*

[2]*Department of Chemical Engineering, Massachusetts Institute of Technology, Cambridge, MA 02139, USA*

[3]*Canadian Light Source Inc., Sakatoon, Saskatchewan S7N 0X4, Canada*

[4]*Pohang Accelerator Laboratory, Jigokro-127-beongil, Pohang, Gyeongbuk 790-834, South Korea*

[5]*Helmholtz-Zentrum Berlin (HZB), Albert-Einstein-Straße 15, Berlin 12489, Germany*

[6]*Department of Mathematics, Massachusetts Institute of Technology, Cambridge, MA 02139, USA*

[7]*These authors contributed equally to this work.*

[8]*Corresponding authors. E-mail: jwlim@snu.ac.kr, bazant@mit.edu*

Abstract

Li-ion battery electrodes exhibit a poorly understood resistance increase during high-rate lithiation, which is rarely observed during delithiation. This hysteresis, often attributed to the solid-state diffusion effect, has not been clearly understood. Here, we unambiguously prove that Li transfer kinetics at the surface determines the overall hysteresis. We use *operando* X-ray microscopy to observe the surface and bulk Li compositions in [100]-oriented Li_xFePO_4 sub-micron particles over a wide range of currents. The experiments reveal how surface and bulk phase separation strongly depend on the direction and magnitude of the current, thereby reconciling contradictions among existing models. The dynamical asymmetry between fast lithiation and delithiation is attributed to autoinhibitory (negative self-feedback on reaction rate) Li-rich and autocatalytic (positive self-feedback) Li-poor domains, respectively. These domains are stabilised in proximity to the active crystal surface. Stabilising electro-autocatalytic surface phases is a promising strategy to enhance the rate capability of Li-ion batteries, as well as lithionic memristors for information storage.

Li-ion batteries (LIBs) are designed for reversible chemical-to-electrical energy conversion.[1] However, at high cycling rates, typically above 1C, there can be significant irreversibility associated with large overpotentials and lost capacity, which is worse during lithiation than delithiation. This phenomenon is more problematic and poorly understood for electrodes undergoing phase transitions, such as $Li_{4/3}Ti_{5/3}O_4$ (LTO)[2] and $LiFePO_4$ (LFP).[3,4] In contrast to solid-solution electrodes, which tend to homogenize the Li distribution for smooth transport within primary particles, phase-separating electrodes exhibit complex, stochastic Li heterogeneity, dividing the active particles into Li-rich and -poor phases during cycling. The local distribution and orientation of dissimilar phases further alter Li transport and (de)insertion rates, as depicted in Fig. 1(a). Owing to difficulty of real-time identification of local Li composition and active areas, various kinetic models[3,5–8] have been limited to demonstrating rate- and path-dependent (de)lithiation kinetics and have not been reconciled. Therefore, it remains unclear how electrochemical conditions, especially at high rates, control (de)lithiation pathways and overall electrochemical impedance.

To test competing kinetic models and reveal the origin of an asymmetric increase in the overpotential during (de)lithiation, it is necessary to simultaneously track the local Li composition evolution and transport rates at the surface and internal regions within individual active particles. The impedance of Li transport during (de)lithiation within the primary particle is fundamentally influenced by the electrode/electrolyte interface charge transfer and bulk Li diffusion process.[9] The kinetics of the two processes strongly depend on the local Li concentration. Therefore, it is desirable to track local Li concentrations at the active surface sites, assess the local rates for each process, and identify the slowest step accounting for the majority impedance to Li transport, *i.e.*, the surface-reaction-limited (SRL) or bulk-diffusion-limited (BDL) processes.

Li_xFePO_4 ($0 < x < 1$), a widely-studied phase-separating material, exhibits strong electrochemical asymmetry in the rate capability and overpotential at high C-rates. As shown in Fig. 1(b), the commercial LFP half-cell shows greater overpotential and lower capacity during galvanostatic lithiation than that during delithiation at higher C-rates while its coulombic efficiency reaches ~100% at a rate of 0.2C. Fig. 1(c) depicts the overpotential applied to the electrode at a state-of-charge (SoC) of 0.5 and indicates that the difference in the overpotential between lithiation and delithiation strongly deviates as C-

rate increases. Many different phase-transformation mechanisms have been proposed for LFP electrodes over the past two decades, including bulk-diffusion-limited shrinking-core[3,5–7,10] with possible amorphisation[11,12], surface-reaction-limited intercalation-wave[8,10,13–16] (or domino-cascade[6,17]) with high-rate quasi-solid-solution[8,18–21], and low-rate coherent surface nucleation[15,22–24] with mosaic instabilities[25–27]. Although each of these scenarios has been supported by experiments and simulations, a unified theory that can explain for the strong asymmetry in overpotential between lithiation and delithiation, indicated in Fig. 1(b), is still needed.

The main experimental challenge lies in resolving the strongly anisotropic transport and reactivity of LFP nanoparticles in liquid electrolyte. As Li diffusion mainly occurs along the [010] direction in LFP,[28–30] it is essential to track Li movement along the [010]-axis of facet-controlled particles in order to distinguish solid-state Li transport and surface charge transfer. Some aspects of Li diffusion along the [010]-axis of micrometre-sized LFP in liquid electrolyte have been visualised using *operando* hard X-ray transmission X-ray microscopy (TXM) by probing Fe K-edge.[6,31] However, tracking complete (de)lithiation along the [010]-axis within the same particle under multiple cycling conditions has not been realised owing to the poor electrochemical performance of battery cells or insufficient spatial/temporal resolution of the microscopy technique. Since hard X-ray TXM has a long probing depth, it cannot provide sufficient absorption contrast for nanoscale particles.

Operando soft X-ray scanning transmission X-ray microscopy (STXM), on the other hand, has emerged as a state-of-art technique that offers much higher chemical sensitivity for nanoparticles, owing to high absorption contrast at the L-edge of the early transition metals. This method enables the imaging of oxidation states with precise quantification and fast temporal resolution, making it effective for unravelling complex (electro)chemical reactions in nanoscale particles in the fields of catalysis and energy storage.[18,32–34] However, the requirement for a vacuum (or He gas) in the STXM X-ray optics presents technical challenges, and Li transport along the [010] direction has only been demonstrated for LFP interfacing with a solid-electrolyte. The use of solid electrolytes, unlike their liquid counterparts, can impose significant stress that may complicate the lattice-elasticity effect and impede complete cycling.[33] Liquid-based *operando* STXM has been successful for the [010]-oriented LFP platelet particles, but it could not capture

solid-state Li transport in the fast [010] Li diffusion channels because the probing beam could only collect depth-averaged Li compositions along the [010] direction.[18]

In this study, we conducted *operando* STXM to simultaneously visualise Li transport at the (de)insertion surface and internal region within [100]-oriented LFP microplatelet single particles (carbon-coated; ~400 nm wide, ~1 μm long, and ~150 nm thick; synthesis details presented in Methods[35,36]) The flat (100) plane allowed the individual particles to lie on the flat current collector of the microfabricated battery cells; therefore, raster-scanning with the focused soft X-ray directly visualised the [010] diffusion channels and the (010) (de)insertion surface regions (*i.e.*, the side edges of the particles) during the battery operations, as shown in Figs. 2(a)–(c).[37] We quantified pixel-wise Li compositions of the LFP particles using Fe L_3-edge absorption spectra, presented in Fig. 2(d) (details in Supplementary Section 4).[9,18,38] Our L_3-edge reference spectra from $LiFe^{2+}PO_4$ and $Fe^{3+}PO_4$ are consistent with previous reports, which explains the shift of both main and minor peaks.[39,40] Under multiple rates of 0.07C–7C (rates below 0.1C, between 0.1C–1C, and above 1C are defined as slow, intermediate, and fast C-rates, respectively), Li transport within ~70 LFP single particles was tracked at ~40 nm spatial and sub-60 s temporal resolutions in 1 M $LiClO_4$ electrolyte in customised microfluidic cells (details in Supplementary Section 1-3). Electrical contacts between the flat plane of the dispersed LFP particles and the current collector were enhanced via carbonisation at 600°C, enabling excellent electrochemical performance of the cells (details in Supplementary Section 1-1 and 1-2).

Representative *operando* STXM results of Li insertion and extraction

Figs. 3(a)–(c) present representative Li composition maps of the [100]-oriented LFP particles obtained from *operando* STXM experiments for 0.15C, 1.5C, and 4C delithiation and 0.15C and 4C lithiation. For 0.15C delithiation (Fig. 3(a)), Li extractions at the particle corner were initiated, while a majority of them were found to exit the [010] diffusion channels before the initiation of extraction from the adjacent channels. This clearly indicates moving phase boundaries between Li-rich and -poor phases (line cuts in Supplementary Fig. 5(a)) parallel to the [010] direction, consistent with intercalation waves[8,13] or domino cascades[17]. This indicates that the small active surface area within the particle can sufficiently accommodate the applied extraction current and that bulk

transport in the activated [010] channels was fast enough to keep up with the focused current. In this regime of anisotropic surface-reaction limitation,[13,21] the characteristic timescale for bulk transport in the [010] direction $\tau_{BT}^{[010]}$ is shorter than that for surface reaction τ_R, which is also shorter than that for bulk transport in the [100] and [001] directions, *i.e.*, $\tau_{BT}^{[010]} < \tau_R < \tau_{BT}^{[100],[001]}$. If inter-channel diffusion along the [100] and [001] directions is much faster than the characteristic reaction rate, then Li transport within the particles is expected to follow pathways controlled by the minimum elastic strain energy, which will be demonstrated in the next section.

In contrast to intercalation-wave features observed at 0.15C delithiation, the majority of (010) insertion surface regions were rapidly populated by Li at 0.15C lithiation, activating most of the [010] channels in the early stage of lithiation, as shown in Fig. 3(a). Compared with delithiation at the same rate, the Li insertion current was no longer focused on a small area fraction within the particles, but spread over a larger surface region. The entire region of the particles became uniformly lithiated, and the slope of the Li concentration gradient (along the [001] direction) was much lower during lithiation than that during delithiation, presenting larger solid-solution domains (line cuts in Supplementary Fig. 5(b)).[8,18,19,21,41,42] Towards the end of lithiation at 0.15C, the Li distribution exhibited a shrinking-core feature with a lower Li concentration at the particle core and diffuse interface between Li-richer and poorer domains.

Both Li insertion and extraction at higher C-rates activate more surface regions and occur more concurrently within the particles, as depicted in Figs. 3(b) and (c). High (de)lithiation currents would stabilise not only the solid-solution phase within the particles, but also Li-rich or -poor phases near the surface region. We note that Li-rich (Li-poor) surface domains formed at high-rate lithiation (delithiation) persists and gradually expand toward the internal region during the overall (de)insertion process, resulting in diffuse shrinking-core features. Interestingly, fast delithiation at 4C bypasses the channel-by-channel reaction pathway at intermediate-rates, while high-rate lithiation drives similar Li pathways but a clearer shrinking-core feature than slower rate lithiation. The results are consistent with a previous study on [010]-oriented LFP particles that observed more uniform Li (de)insertion as C-rate increases, supporting the robustness of our measurement platform.[18] We demonstrate that local Li composition both at the surface and internal region in LFP are strongly dependent on current rates and directions as well as

inhomogeneous. Moreover, our results successfully reconcile competing models at various C-rates, and present the fundamental difference between high-rate lithiation and delithiation, *i.e.*, the surface Li composition. Finally, the observed surface Li composition at multiple C-rates does affect the overall rates of (de)lithiation process as a source of the significant electrochemical asymmetry, which will be further discussed in the last section.

(De)lithiation governed by SRL process at intermediate and slow C-rates

In contrast to BDL process, the current density j within the single particles is strongly coupled with the surface Li composition in SRL regime.[18] In this sense, we calculated the local Li (de)insertion rates applied to the [010] channels while tracking the local Li composition at the (010) reaction surface region at intermediate C-rates. In the schematics in Fig. 4(a) (top), mean (de)lithiation rate $\Delta x/\Delta \mathrm{t}$ between two sequential Li composition maps of [100]-oriented LFP particle is depicted (Δx: pixel-wise Li composition difference, $\Delta \mathrm{t}$: time interval $\mathrm{t}_2 - \mathrm{t}_1$). Because Li-ion transfer and Li diffusion primarily occur respectively at the (010) surface and along the [010] channels for the reaction timescale of our study, integrating $\Delta x/\Delta \mathrm{t}$ along the [010] channel yields the local current density applied to the channel, as plotted in the current density histogram. In our works, a straight line of ~40 nm pixels along the [010] direction was termed a pixelated channel (Ch) (refer to Supplementary Section 6), and j_{Ch} is the current density applied to the Chs (details in Supplementary Section 11).

In Fig. 4(a) (bottom), the local current density j_{Ch} is extracted from the x and $\Delta x/\Delta \mathrm{t}$ maps of the representative particle during 0.15C (de)lithiation. Blue-solid and red-dotted line in the graph in Fig. 4(a) indicate the current density applied to each Ch j_{Ch} (yellow box in $\Delta x/\Delta \mathrm{t}$ map) and surface Li composition (pink boxes in surface Li composition map), respectively. The j_{Ch} line profile during lithiation is distributed more homogeneously than that during delithiation, agreeing with a shrinking-core pathway and intercalation wave pathway during lithiation and delithiation, respectively. The correlation of the line profiles between j_{Ch} and surface lithium composition shows that j_{Ch} increases (decreases) as surface lithium decreases (increases), indicating that lithium-deficient surfaces can enhance the local current density.

To further understand the intrinsic reaction rate constant at the surface, we calculated the local exchange current density of Chs. From j_{Ch}, the local exchange current

density of the Chs (j_0) was then extracted by assuming a linear relationship between current and voltage for small overpotentials <120 mV (Supplementary Section 11).[18,43] In Fig. 4(b), the normalised exchange current density $\tilde{j}_0$ for the selected Chs is plotted as a function of the surface Li composition for each Ch $\langle x_{Ch}^{surf} \rangle$ (Supplementary Section 6). Within the regime of SRL, the surface Li composition could play a crucial role in regulating the rates of Li insertion and extraction. Specifically, in autoinhibitory reaction regime, lithiation at the surface region leads to a reduction in Li insertion rates due to the greater Li population (i.e., negative feedback). Conversely, in autocatalytic reaction regime, delithiation at the surface region promotes Li extraction rates due to the lower Li concentration (i.e., positive feedback). The phenomenon of electro-autocatalysis[20,44,45] is evident for 0.15C cycling, where autoinhibitory and autocatalytic trends in the reaction kinetics (via $\tilde{j}_0$) lead to more homogeneous, decelerating lithiation, and more heterogeneous, accelerating delithiation, respectively.[18,20,21,46–48] As the Chs upon delithiation increase the rate capability and accommodate a higher current, the adjacent channels are not activated until the fast Chs complete delithiation, yielding a domino-cascade feature. In contrast, as the lithiation of Chs decreases the rate capability, more surfaces and channels must be activated to accommodate the applied current, resulting in a diffuse shrinking-core feature. These observations appear to be the first to capture such autocatalytic and autoinhibitory (de)insertion kinetics from identical nanosized domains under multiple cycling conditions.

To extend our kinetic understanding to near-equilibrium dynamics where the asymmetry between lithiation and delithiation should be reduced, we further performed *operando* STXM at extremely slow rates of 0.07C lithiation and 0.09C delithiation, as shown in Fig. 4(c). Sharp phase boundaries between the Li-rich and -poor domains developed along the diagonal (white dashed lines in Fig. 4(c)), as observed in the relaxed particles at equilibrium (Fig. 3(d)). These boundaries slowly propagated in the direction normal to the interface during (de)lithiation. Contrary to observations at the intermediate rate (*e.g.,* 0.15C), the phase transformation kinetics of lithiation and delithiation were indistinguishable and exhibited symmetric features. Additionally, line cuts of the Li composition across the phase boundaries in Fig. 4(c) present clear intercalation waves that were not detected at 0.15C lithiation.

Our three-dimensional phase-field simulation for slow (de)lithiation at ~0.03C,

presented in Fig. 4(d), successfully describes the *operando* Li maps at near-equilibrium rates in Fig. 4(c). Moving phase boundaries with tilted angles were captured in the simulation, which are driven by the anisotropic misfit strain between two immiscible phases.[46] The elastically driven phase boundaries were stably formed even after relaxation, as captured in the simulation in Supplementary Fig. 12. To maintain the angles of boundaries during (de)lithiation, bulk Li transport must occur along all directions at the given reaction timescale for attaining the interface of minimum elastic strain energy. Because diffusion coefficients of Li-vacancies are extremely anisotropic in LFP, $D_{[010]}$≈10^{-9} cm^2/s and $D_{[100]/[001]}$ ≈10^{-14} cm^2/s at 300 K,[28,49] characteristic diffusion times for ~200 nm length in the [010] and [100]/[001] direction were ~0.4 s and ~11 h, respectively. Interchannel diffusion along the [100] or [001] direction can be enhanced at Li-deficient domains or by the effect of surface Li diffusion mechanism.[9,50] Therefore, sufficient time for bulk transport was allowed in all directions during the given (de)lithiation time at ~0.08C (~12.5 h), supporting that Li (de)insertion reaction was observed at slow C-rates exists in the regime of isotropic SRL process, $\tau_R > \tau_{BT}^k$ (k = [100], [010], and [001]).[13] From this observation, we connect the near-equilibrium dynamics of Li transport within the single particles with highly non-equilibrium kinetics, which were only partially captured in previous investigations.[6,9,18,33] Additionally, the fact that the particles considered in this study followed an elastically driven pathway rules out any complexity originating from minor crystalline defects, such as extended defects or grain boundaries (supported by Supplementary Section 3).

Concurrent and active phase transformations of the surface region at higher C rates

Transient Li maps at high C-rates were further analysed to reveal the origin of the significant asymmetry in overpotential and rate-capability between lithiation and delithiation. Fig. 5(a) shows representative Li composition maps captured near an SoC of 0.5 during *operando* STXM at 4C lithiation and 7C delithiation. Li-rich (-poor) domains at the nanoscale surface regions were clearly developed during lithiation (delithiation), presenting clearer diffuse shrinking-core features. The composition difference between core and shell regions was manifested by varying current rates and directions, which could not be demonstrated by previous investigations. Notably, such Li distributions at the surface region were persistent and slowly decomposed to end phases during relaxation, as shown

in Supplementary Fig. 8(a). Meanwhile, high-rate (de)lithiation currents also increased the solid-solution fraction and Li uniformity coefficients within the particle, as supported in Supplementary Fig. 9(c).

Addressing the rate-determining step (RDS) of the captured (de)lithiation pathways would shed light on whether surface reaction or bulk transport is responsible for the large electrochemical asymmetries observed at high C-rates. Caution is to be exercised while determining the RDS in phase-separating materials because both BDL and SRL regimes can exhibit confusingly similar transport patterns. Li (de)insertion under BDL regime activates the entire reaction surface and renders a sharp diffusional front near the surface region, which is extremely (de)lithiated during (de)insertion with clear interfacial boundaries.[10,48] Likewise, in the SRL regime, phase-separating materials also exhibit biphasic or multiphasic Li inhomogeneity and accordingly generate sharp phase boundaries anywhere within the particle.

There exists evidence suggesting that the overall dynamics do not agree with BDL regime, but are consistent with the SRL regime, even at the highest C-rates. First, as presented in the previous section, the characteristic diffusion time of Li-vacancies in ~200 nm [010] channels was ~0.4 s, much faster than the cycling time (~8.5 min) at 7C delithiation. Second, the Li composition at the (010) surface does not reach zero at the midstage of 7C delithiation, as shown in Supplementary Fig. 8(b), indicating that sufficient Li ions at the surface can be readily extracted. In BDL regime, surface Li should be significantly depleted or populated and be hardly replenished via bulk transport, especially in phase-separating materials.[10] Third, composition gradients near the surface region are extremely broad and present a solid-solution domain (a fingerprint of SRL), whereas slow diffusion generally renders an abrupt wavefront in BDL regime.[48] Additionally, the broad interface does not result from the microscopy resolution, which can resolve the sharp boundaries presented in Fig. 4(c) at low C-rates.

To further prove that the particles at fast C-rates were in SRL regime, the LFP particle with a pre-delithiated core was delithiated at 4C for *operando* STXM (Supplementary Fig. 7(a)). The existence of pre-delithiated core domains can lower the barrier for early transition to Li-poor phases. This would allow us to locate the positions of Li ion extraction from the early stage of delithiation and distinguish the difference between SRL and BDL, as depicted in Supplementary Fig. 7(d). Thus, the governing kinetics can

be resolved without interference from surface phase transitions. In BDL regime, Li concentration at the surface region should be depleted at fast delithiation. However, herein 4C delithiation gradually expanded the pre-delithiated core to the edge and did not deplete Li concentration at the surface region assisted by fast diffusion in the [010] direction. Therefore, we conclude that our observations at fast C-rates fall within SRL regime.

As such, surface reaction rates, controlled by Li composition at the active surface, govern the overall (de)insertion reaction kinetics. Therefore, Li compositions at the surface region $\langle x_{\mathrm{surf}} \rangle$ and the internal region $\langle x_{\mathrm{internal}} \rangle$ of the single particles at an SoC of 0.5 (defined in Supplementary Section 6) were calculated as a function of the C-rate and are shown in Fig. 5(b). According to the correlation between $\langle x_{\mathrm{surf}} \rangle$ and $\tilde{j}_0$, addressed in Fig. 4(b), the left and right y-axes in Fig. 5(b) denote $\langle x \rangle$ and $\tilde{j}_0$, respectively. Remarkably, $\langle x_{\mathrm{surf}} \rangle$ becomes Li-richer (Li-poorer) with increasing lithiation (delithiation) rates, while $\langle x_{\mathrm{internal}} \rangle$ shifts in the opposite direction. Specifically, $\langle x_{\mathrm{surf}} \rangle$ at an SoC of 0.5 became ~0.64 and ~0.41 during 4C lithiation and delithiation, respectively, where each value corresponds to $\tilde{j}_0$ ~0.52 and ~0.87 according to the skewed $\langle x_{\mathrm{surf}} \rangle - \tilde{j}_0$ relation in Fig. 4(b). Therefore, high-rate delithiation could drive a greater j_0 at the surface region, while high rate lithiation was found to reduce it. Especially in the case of delithiation, the greater rate-capability resulting from Li-deficient domains might be responsible for the slow decline in the trend of Li composition above 4C in Fig. 5(b).

The surface pixels were categorised into the ‘active’ and ‘transformed’ groups according to the Li concentration: The active pixel is defined as the Li concentration in the range of $0.15 \leq \langle x_{\mathrm{surf}} \rangle \leq 0.85$, whereas the transformed pixel is defined as the Li concentration in the range of $\langle x_{\mathrm{surf}} \rangle \leq 0.15$ for delithiation and $\langle x_{\mathrm{surf}} \rangle \geq 0.85$ for lithiation. Fig. 5(c) indicates the fraction of the active/transformed population of the surface pixels at an SoC of 0.5 as a function of C-rates. At 0.15C, lithiation induced a greater active fraction (solid-solution fraction) of the surface pixels than delithiation (Fig. 3(a)), consistent with the results from the autoinhibitory reaction at the surface within the single particles.[20,21,51] At higher rates, the active and transformed fraction increased and reached ~90% and ~10%, respectively, at 4C (de)lithiation. It indicates that the surface regions are clearly distinguished from the inner region and allows concurrent Li-ion insertion/extraction. Delithiation at higher rates lowers $\langle x_{\mathrm{surf}} \rangle$ and activates a larger surface area which accelerates Li extraction from the particles and decreases the impedance. In contrast,

significant surface activation was already induced by lithiation at intermediate rates and becomes saturated at high rates. As lithiation at high rate increases $\langle x_{\mathrm{surf}} \rangle$, Li insertion decelerates, and the electrochemical impedance increases. Thus, it results in the large gap in the overpotential and rate capability during high-rate (de)lithiation, observed in Fig. 1. Increasing impedance of the individual particle kinetics at high lithiation rates can lead the more particles to be activated to accommodate the large current in the porous electrode compared with delithiation. Our explanation agrees with previous experimental observations and theoretical predictions that more particles are activated during lithiation in LFP porous electrodes, while the active population remains relatively constant during delithiation with increasing C-rates.[27,45]

Beyond the original quasi-solid-solution picture[8,18,46] we propose a new (de)lithiation pathway in LFP, where solid-solution phase evolution over the entire particle and concurrent phase transformation at the surface region occur simultaneously at high C-rates. In the previous solid-solution model in LFP, a uniform Li composition of $\langle x \rangle$=0.5 throughout the particles induced by fast cycling is expected to have same reaction rates during lithiation and delithiation, and could not properly explain asymmetric overpotential at an SoC of 0.5.[18]

Fig. 6 shows how Li transport pathways in LFP change as the (de)lithiation rates increase. At intermediate rates, the asymmetry in Li composition between delithiation and lithiation occurs within individual particles. During delithiation, the Li extraction current is applied to a small surface area, and the surface with a lower concentration enables more Li to be rapidly extracted through the [010] channels due to electro-autocatalytic nature of Li deinsertion reaction. The exit of most Li from these activated channels triggers delithiation of adjacent (010) surfaces and [010] channels, resulting in intercalation-wave kinetics. In contrast, during Li insertion, nearby surfaces and channels start lithiation before the activated channels are fully lithiated. This is due to the auto-inhibited nature of Li insertion reaction. While bulk Li transports along the [010] channels are fast and can keep up with the Li insertion flux, lithiation currents spread over a larger surface area, resulting in shrinking-core features that become noticeable near the end of lithiation process.

At faster (de)lithiation rates, the higher current density activates most of the surface regions, where $\langle x_{\mathrm{surf}} \rangle$ becomes Li-richer for lithiation and -poorer for delithiation.

High (de)lithiation currents kinetically stabilise such phase-separated surfaces, which persist even after an hour of relaxation. Under the SRL regime, these surface phases govern Li (de)insertion rates at the surface and thus contribute to the strong hysteresis in overpotential and rate-capability between lithiation and delithiation. Kinetically phase-separated surfaces, such as those found in LFP, may also occur in other electrodes that undergo phase transitions and have sluggish lithiation kinetics compared to delithiation.

Concluding remarks

In this study, we visualised anisotropic and rate-dependent phase-transformation pathways, reconciled existing Li transport models for LFP, and revealed the origin of asymmetry in the overpotential and rate capability between fast lithiation and delithiation. The results highlight the importance of distinguishing between surface and bulk Li concentration profiles. By modulating the nucleation energy barrier of Li-rich phase on the surface of the active material through techniques, such as amorphization,[52] coating, doping, and others, optimal electro-autocatalysis can be achieved during cell operation. This can improve the rate capability and minimize the asymmetry between ultra-fast charging and discharging. These results could provide insights into the behavior of other LIB electrodes, such as $LiCoO_2$ (LCO),[53] $LiNi_{1/3}Mn_{1/3}Co_{1/3}O_2$ (NMC111),[54] Li-Mn-rich NMC,[55] which often exhibit a greater overpotential during lithiation than during delithiation. Moreover, our study may also have applications in lithionic memristors[56,57] that can store information by modulating the electronic conductivity of Li surface phases (*e.g.*, in LTO[58] and LCO[59]), which have to be visualised at the nanoscale.

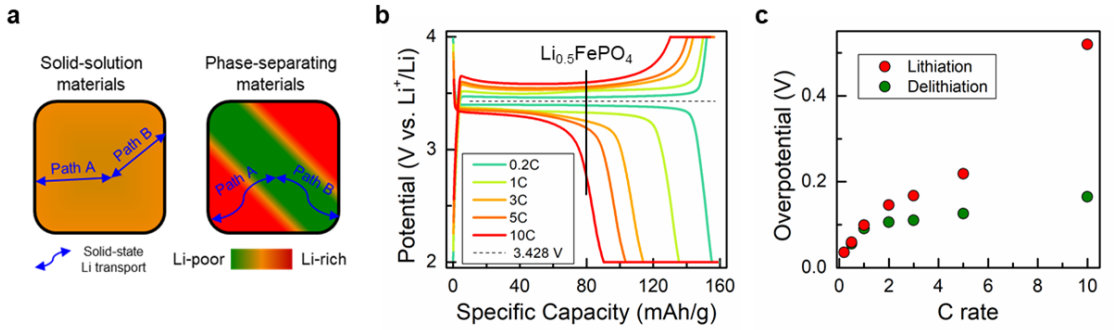

Fig. 1 Schematics of Li transport pathways and typical electrochemical properties of constant current/voltage (de)lithiation for LFP (MTI Corporation)/Li electrode. **a**, Schematics of solid-state Li transports in solid-solution (left) and phase-separating (right) materials. Path A and Path B show possible transport pathways where those in phase-separating materials have more anisotropy and spatial dependency. **b**, Rate-dependent galvanostatic profiles of $LiFePO_4$/Li electrode. Horizontal dashed- and vertical solid- line indicate the middle of 0.2C lithiation/delithiation plateau, 3.428 V, and the half-cycled capacity, $x = 0.5$ of Li_xFePO_4, respectively. **c**, Overpotential with respect to 3.428 V at $x = 0.5$ as a function of C-rate. The overpotential increase during lithiation (red) is much greater than that during delithiation (green) at higher rates.

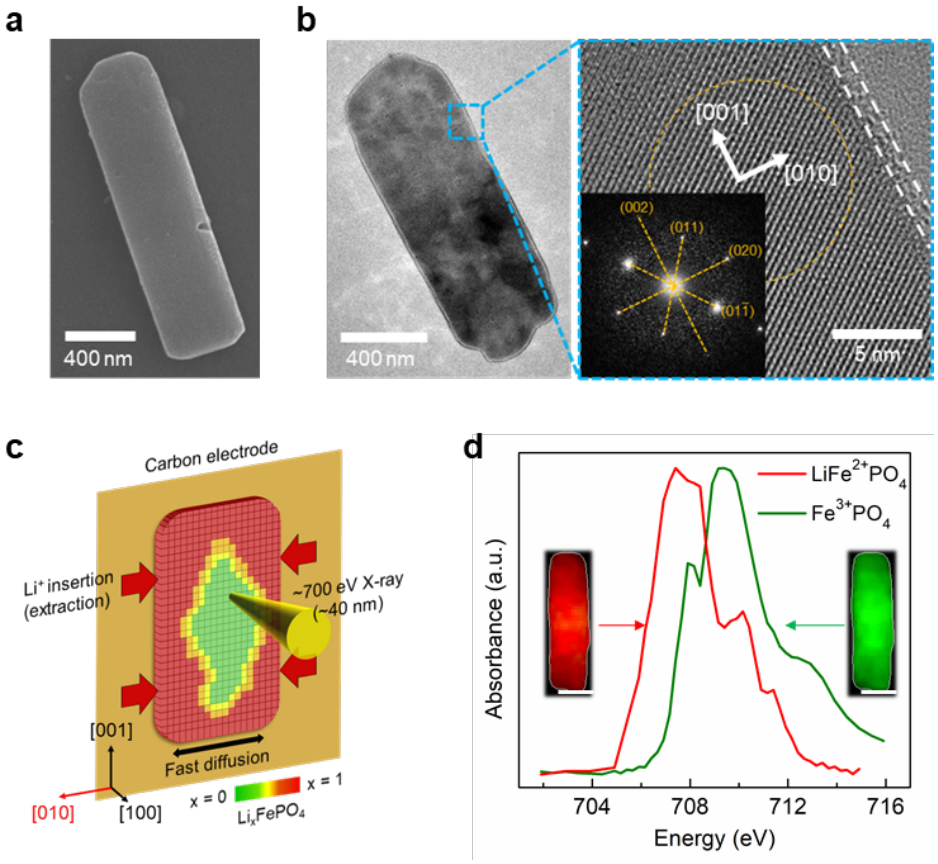

Fig. 2 Electron microscopy images of [100]-oriented $LiFePO_4$ (LFP) primary particle and *operando* STXM imaging schematic. a, SEM image of the (100) plane of a primary LFP particle. **b**, TEM, and HRTEM image of [100]-oriented LFP particle along the [100] zone axis. The inset is the local Fast Fourier Transformation pattern of the selected area, orange dashed circle. **c**, A schematic of *operando* STXM imaging of the LFP/C electrode in EC/DMC electrolyte. Probing beam is ~700 eV monochromatic x-ray focused down to ~ 40 nm. **d**, Soft x-ray absorption spectra of $LiFe^{2+}PO_4$ and $Fe^{3+}PO_4$ single particle at L_3-edge in the electrolyte. Red and green indicate Li-rich and -poor phase, respectively.

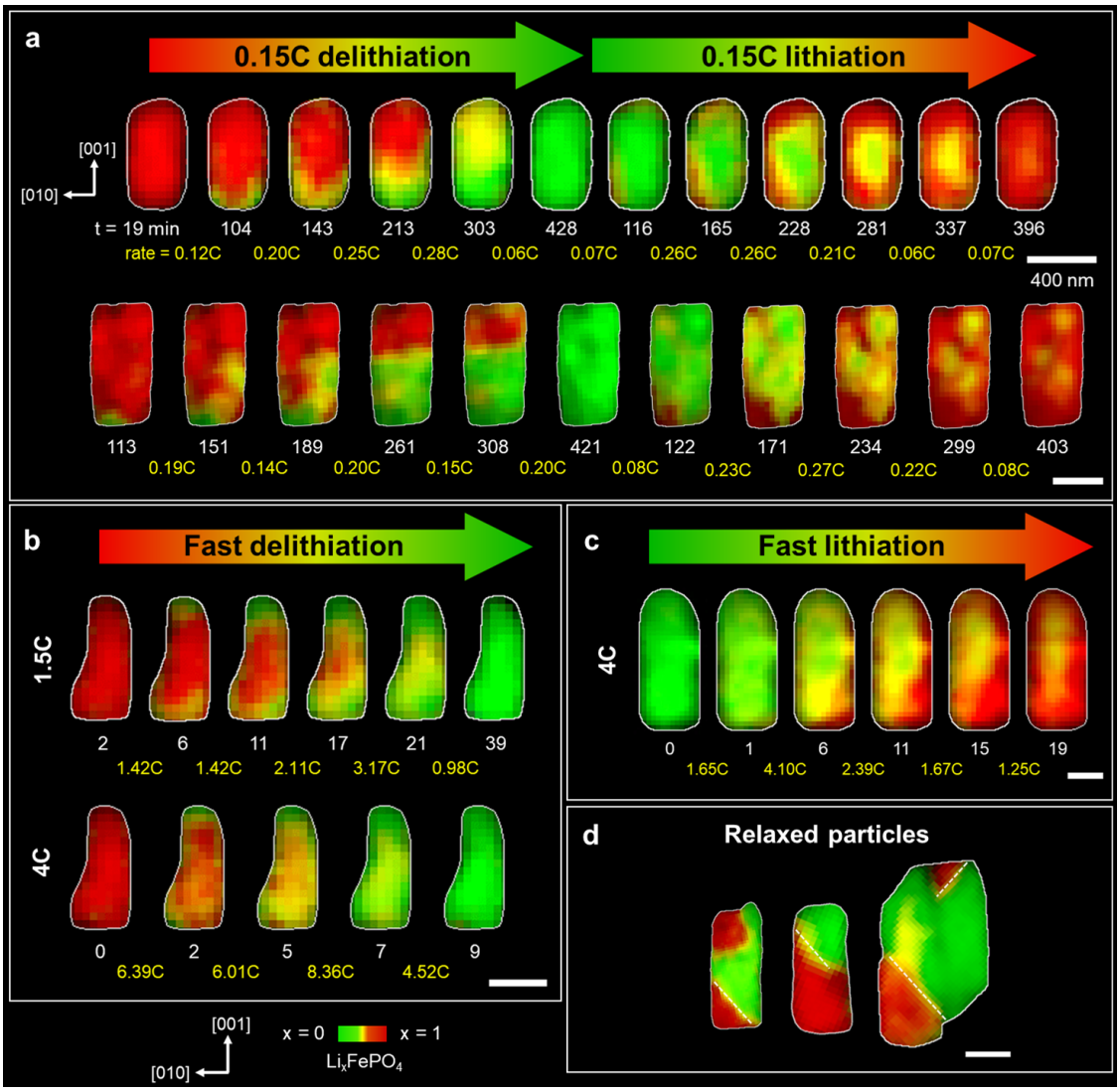

Fig. 3 Representative *operando* STXM results of [100]-oriented Li_xFePO_4 primary particles. a, Li composition maps of two representative particles during electrochemical (de)lithiation process at 0.15C. **b**, **c**, Li composition maps at higher rates delithiation (1.5C, 4C), and lithiation (4C). Hue in each frame represents Li-rich (red) and Li-poor (green) phase, respectively. White and yellow numbers below each frame indicate electrochemical cycling time in minute and interval reaction rate, respectively. **d**, Ex-situ Li composition maps of relaxed particles over 3 months. All frames are rotated with respect to the particle morphology where the vertical axis is parallel to [001] direction. Scale bars, 400 nm.

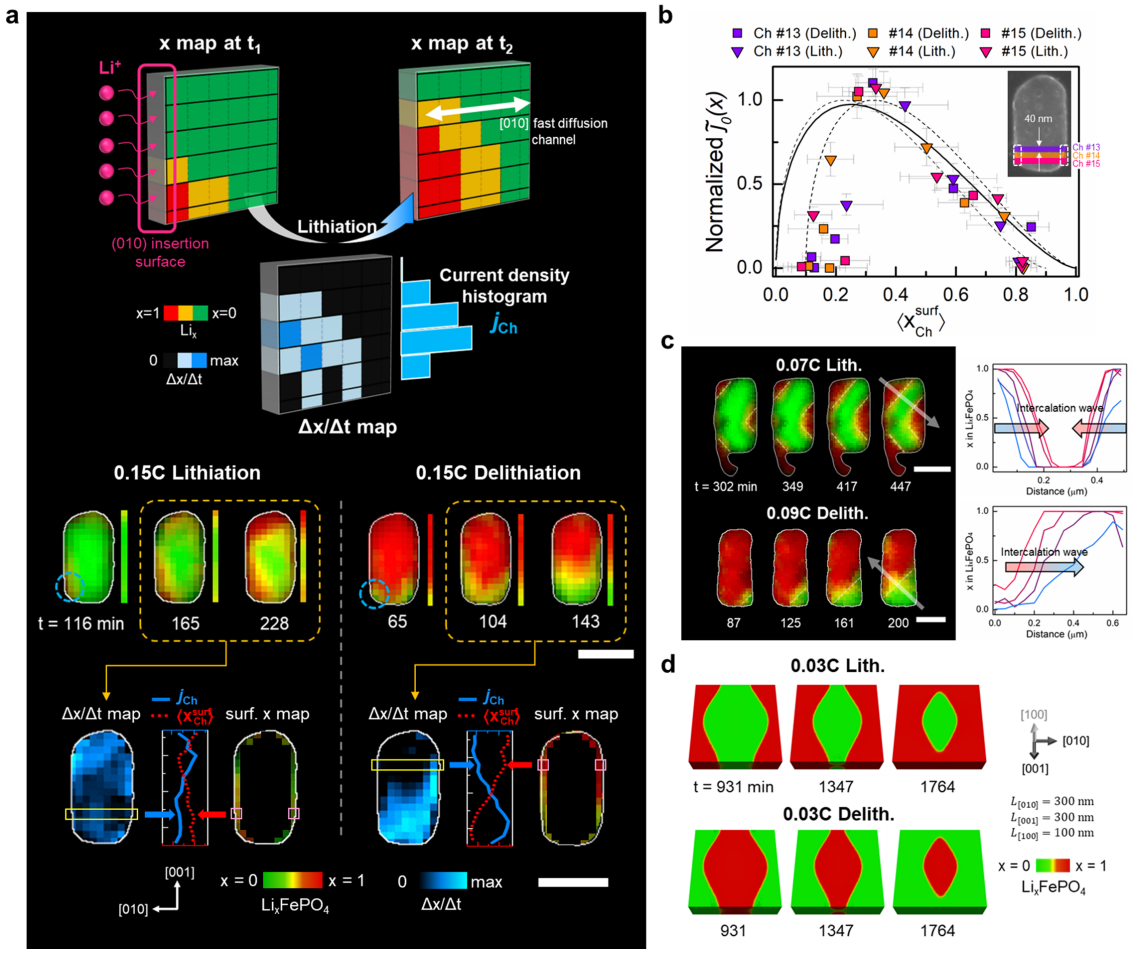

Fig. 4 Analysed Li (de)insertion kinetics at intermediate (a, b) and slow (c, d) reaction rates. a, (Top) Schematics for relationships of the Li composition (x) evolution, local (de)lithiation rate (blue-coloured map; $\Delta x/\Delta t$), and (de)insertion current density applied to each Ch (j_{Ch}). j_{Ch} is calculated by integrating $\Delta x/\Delta t$ along the Ch. (Bottom) x and $\Delta x/\Delta t$ colormaps of the representative particle, and the line profiles of j_{Ch} (blue-solid) and the surface Li composition $\langle x_{Ch}^{surf} \rangle$ (red-dotted) in the inset graph. **b**, Normalised exchange current density $\tilde{j}_0(x)$ of the selected Chs (#13, #14, and #15) in the particle in (**a**) as a function of Li composition of the surface pixels in each Ch $\langle x_{Ch}^{surf} \rangle$. Here, the selected Chs are coloured in purple, orange, and pink respectively, and the pixels for $\langle x_{Ch}^{surf} \rangle$ are marked by white-dashed box in the inset SEM image. The black-solid line is the skewed function of $\tilde{j}_0(x)$ (see Supplementary Section 11) and the dashed-line is the shifted skewed function due to uncertainties arising from averaging $\langle x \rangle$ of the surface pixels. **c**, (Left) Li maps of representative particles at very slow C-rates, 0.07C for lithiation and 0.09C for delithiation. (Right) Line cuts of Li composition along the white

arrows. **d**, 3D phase-field simulations during ~0.03C (de)lithiation of [100]-oriented LFP particle (details in Supplementary Section 12). Scale bars, 400 nm.

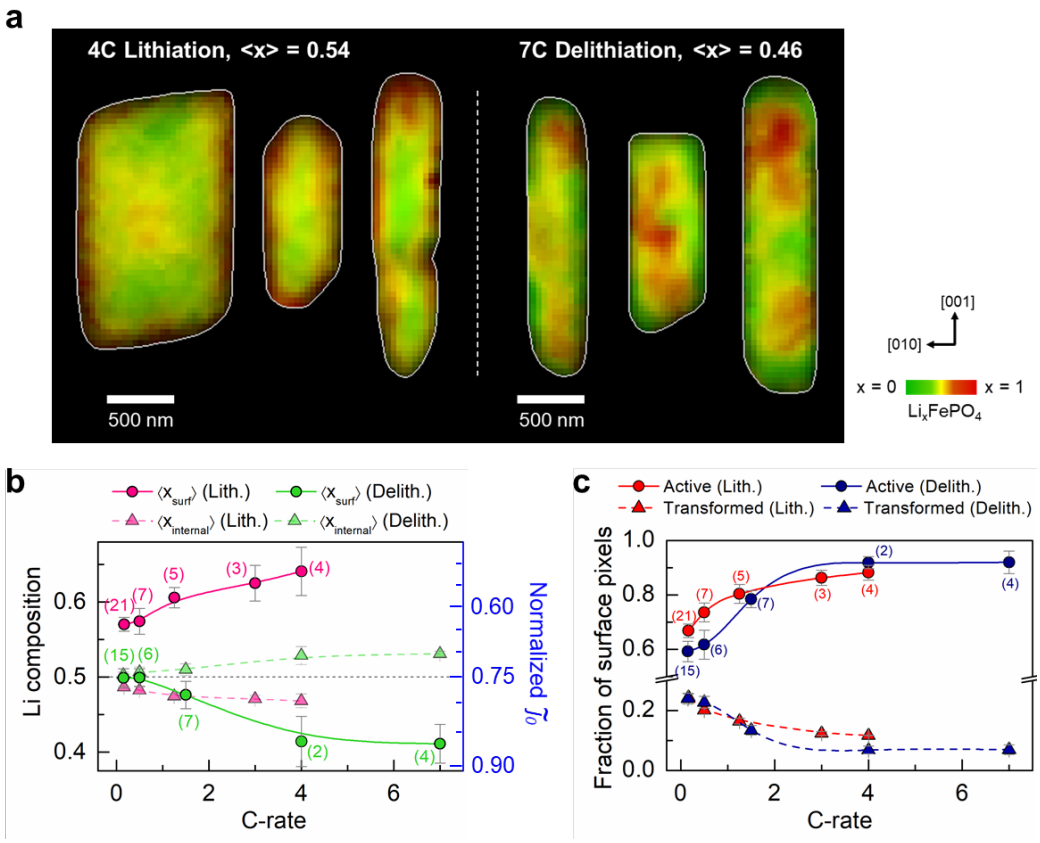

Fig. 5 *Operando* STXM results at higher rates nearly at SoC 0.5, and analysis of the surface and internal pixels at SoC 0.5. a, Li composition maps captured approximately at SoC 0.5 state during 4C lithiation and 7C delithiation. Higher C-rate lithiation and delithiation induce more lithiated and delithiated surface of LFP particles, respectively. **b**, $\langle x_{surf} \rangle$ (circle, solid line) and $\langle x_{internal} \rangle$ (triangle, dashed line) of the single particles as a function of global C-rate. **c**, Population fractions of the active (circle, solid line) and transformed (triangle and dashed line) surface pixels as a function of C-rate. The active pixel is defined as the pixel at $0.15 \leq \langle x_{surf} \rangle \leq 0.85$, and the transformed is defined as the pixel at $\langle x_{surf} \rangle \leq 0.15$ for delithiation and $\langle x_{surf} \rangle \geq 0.85$ for lithiation. The values in parentheses in (**b**) and (**c**) indicate the number of well-faceted particles captured at the same electrochemical rate.

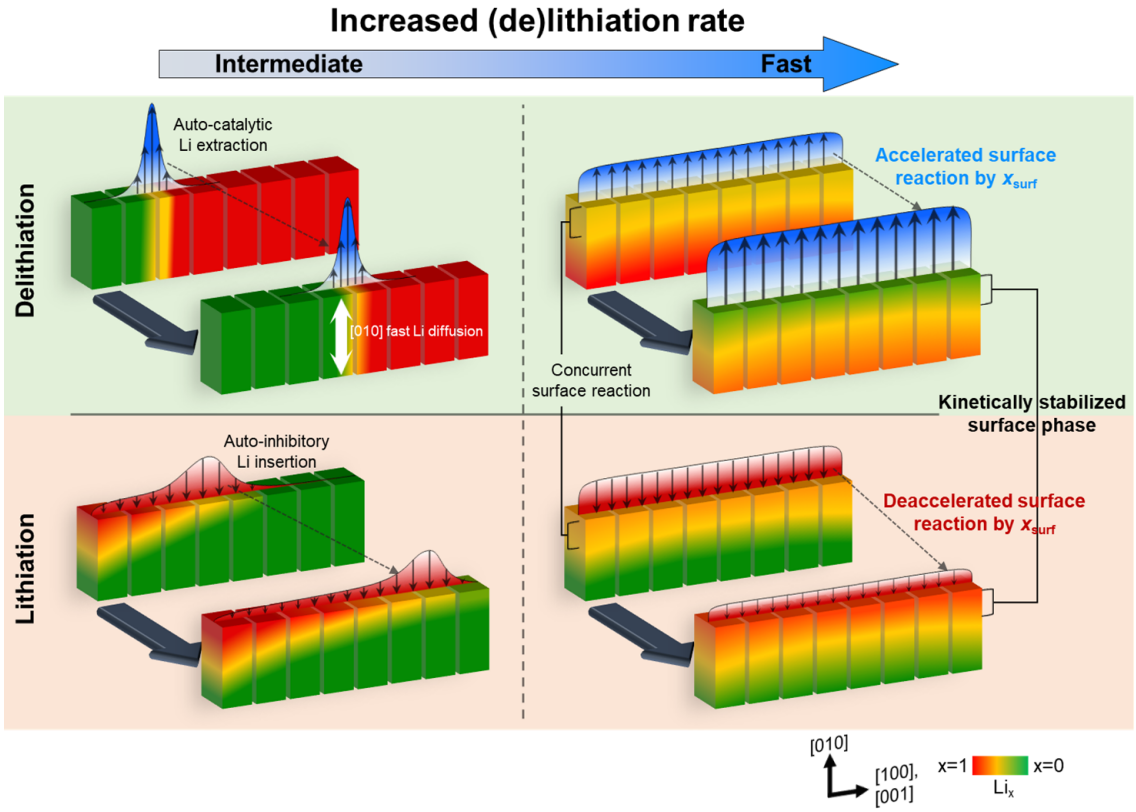

Fig. 6 Pathway of Li (de)insertion, influenced by reaction rates. At intermediate rates, the asymmetric phase evolution of (de)lithiation within a particle is driven by autocatalytic and autoinhibitory surface reactions. During delithiation, the extraction of Li begins with a small surface and [010] channel, followed by the activation of the adjacent [010] channels. This channel-by-channel Li extraction continues throughout the delithiation process, resulting in an intercalation wave or domino-cascade feature. In contrast, at intermediate rates, lithiation currents rapidly spread over a larger surface area than delithiation currents, leading to a diffuse shrinking-core feature at the end of lithiation process. At high rates of Li (de)insertion, the surfaces are concurrently activated and become Li-poorer during delithiation and Li-richer during lithiation. A kinetically stabilised Li-poor (Li-rich) surface further boosts (impedes) the delithiation (lithiation) process.

Methods

Synthesis. [100]-oriented $LiFePO_4$ (LFP) microplatelet particles was synthesised based on the following procedures. First, anhydrous Li_3PO_4 powders were prepared by neutralisation reaction of H_3PO_4 (≥ 85 % wt. in H_2O, SigmaAldrich) and LiOH (98%, Alfa Aesar). 16 mmol of H_3PO_4 was added dropwise within 5 minutes in to the 100 mL aqueous solution of 50 mmol of LiOH (dissolved in 100 mL de-ionised water) under magnetic stirring (250 rpm), followed by white suspension. After the stirring at room temperature for another 15 minutes, the resulted suspension was collected through centrifugation (4500 rpm, 5 times) and washed with DI water, and finally dried at 110 °C for 12 h. $FeSO_4·H_2O$ powders were prepared by heat treatment of $FeSO_4·7H_2O$ (≥ 99 %, SigmaAldrich) at 100 °C for 12 h under vacuum condition.[35]

Using a solvothermal method, Li_3PO_4 (0.4300 g, 3.71 mmol) was added to a solution with 2.5 mL ethylene glycol (99.8 %, SigmaAldrich) and 2.5 mL DI water. Then, 1.85 mmol of H_3PO_4 was subsequently added to the first solution. $FeSO_4·H_2O$ (0.5641 g, 3.71 mmol) was added to another solution of 2.5 mL ethylene glycol, 2.5 mL DI water, and 0.11 mmol of L-Ascrobic acid (≥ 99 %, SigmaAldrich). The L-Ascorbic acid is included in the synthesis to decreases the pH of precursor solution, which promotes the development of the [100] orientation of LFP platelet particles. After fully dissolving of a precursor in each solution, two solutions were mixed (molar ratio of Li:Fe:P = 3:1:1.5) for 15 minutes under magnetic stirring in a Teflon liner (500 rpm). The Teflon liner was transferred to autoclave and heated in a KF-96 Polydimethylsiloxane oil bath up to 180 °C holding for 2 h under magnetic stirring (800 rpm). The consequent suspension was collected through centrifugation (4500 rpm) and washed with DI water (4 times) and anhydrous ethanol (1 time), and dried at 110 °C for 12 h.

Electrochemistry. For electrode slurry, the active materials (LFP, MTI Corporation), carbon black (Super P, TIMCAL), binder (polyvinylidene fluoride) were homogeneously mixed in 7:2:1 weight ratio with N-methylpyrrolidone (NMP, Acros Organics, 99%) using a planetary mixer. The slurry and casted onto carbon-coated aluminium foils with ~20 µm thickness using a doctor blade method, and the casted slurry was dried on a hotplate at 80 ºC overnight and then calendared. The final thickness of the composite is less than ~20 µm. CR2032-type coin cells were used in Fig. 1, where Li foil anode, Celgard 2320 separator, and 1M $LiPF_6$ in EC and DMC mixture (50%:50% in volume ratio) electrolyte

were assembled. For the rate-capability test, LFP/Li cells were intentionally cycled under the constant current and potential steps to drive the electrode fully (de)lithiated at the end of the cycle, and to monitor overpotentials when the (de)lithiation starts from the complete Li-rich and poor states of the electrode. The cut-off of the constant potential step at 4V and 2V condition was when the absolute current is less than 0.05C.

Scanning Transmission X-ray Microscopy (STXM). We conducted *operando* and ex-situ STXM experiments at Fe L_3-edge absorption ~710 eV. The experiments were performed at beamline 10ID-1 at Canadian Light Source Beamline, 10A-1 at Pohang Accelerator Laboratory, and MYSTIIC at BESSY II Helmholtz Zentrum Berlin. The subtle energy difference between each beamline was calibrated by Fe^{2+} absorption spectrum of pristine LFP particle.

TEM and HR-TEM. TEM images were obtained by Talos F200X at an accelerating voltage of 200 kV.

Acknowledgements J. Lim acknowledges support from the Samsung Science and Technology Foundation under project no. SRFC-MA2002-04. B.K. is supported by National Research Foundation of Korea (NRF) Grant funded by the Korean Government (NRF-2019-Global Ph.D. Fellowship Program). C.N. is supported by Fellowship for Fundamental Academic Fields funded by Seoul National University. D.F., H.Z., N.N., and M. Z. B acknowledge the Toyota Research Institute through the D3BATT Center on Data-Driven-Design of Rechargeable Batteries.

Author contribution B.K., J.C., J.K. and J.L. designed the concept of experiments and performed STXM experiments. B.K. performed the overall STXM data analyses, conducted theoretical study through 2D phase field simulation with C.N., and wrote the manuscript. J.C. designed microfabricated chips and optimised chip-particle contact. J.K. synthesised [100]-oriented microplatelet LFP single crystals and performed electrochemical measurements for LFP coin cells. S.S. conducted ex-situ XRD and its analysis. J.H. measured TEM images. D.L. and S.J. supported *operando* STXM experiments. D.F. developed 3D phase field simulation of LFP. D.F., H.Z., and N.N. contributed to crucial discussions

of the simulation under the supervision by M.Z.B. J.L and M.Z.B supervised this work. All authors contributed to the discussion of the results.

References

1. Goodenough, J. B. & Park, K. S. The Li-ion rechargeable battery: A perspective. *J. Am. Chem. Soc.* **135**, 1167–1176 (2013).
2. Takami, N., Hoshina, K. & Inagaki, H. Lithium Diffusion in Li 4/3 Ti 5/3 O 4 Particles during Insertion and Extraction . *J. Electrochem. Soc.* **158**, A725–A730 (2011).
3. Srinivasan, V. & Newman, J. Existence of path-dependence in the LiFePO 4 electrode. *Electrochem. Solid-State Lett.* **9**, 110–114 (2006).
4. Chong, J. *et al.* Towards the understanding of coatings on rate performance of LiFePO 4. *J. Power Sources* **200**, 67–76 (2012).
5. Srinivasan, V. & Newman, J. Discharge Model for the Lithium Iron-Phosphate Electrode. *J. Electrochem. Soc.* **151**, A1517 (2004).
6. Wang, J., Chen-Wiegart, Y. C. K. & Wang, J. In operando tracking phase transformation evolution of lithium iron phosphate with hard X-ray microscopy. *Nat. Commun.* **5**, 1–10 (2014).
7. Padhi, A. K., Nanjundaswamy, K. S. & Goodenough, J. B. Phospho-olivines as Positive-Electrode Materials for Rechargeable Lithium Batteries. *J. Electrochem. Soc.* **144**, 1188–1194 (1997).
8. Malik, R., Zhou, F. & Ceder, G. Kinetics of non-equilibrium lithium incorporation in LiFePO4. *Nat. Mater.* **10**, 587–590 (2011).
9. Li, Y. *et al.* Fluid-enhanced surface diffusion controls intraparticle phase transformations. *Nat. Mater.* **17**, 915–922 (2018).
10. Fraggedakis, D. *et al.* A scaling law to determine phase morphologies during ion intercalation. *Energy Environ. Sci.* 22–27 (2020).
11. Kao, Y. H. *et al.* Overpotential-dependent phase transformation pathways in lithium iron phosphate battery electrodes. *Chem. Mater.* **22**, 5845–5855 (2010).
12. Tang, M. *et al.* Model for the particle size, overpotential, and strain dependence of phase transition pathways in storage electrodes: application to nanoscale olivines. *Chem. Mater.* **21**, 1557–1571 (2009).

13. Singh, G. K., Ceder, G. & Bazant, M. Z. Intercalation dynamics in rechargeable battery materials: General theory and phase-transformation waves in LiFePO4. *Electrochim. Acta* **53**, 7599–7613 (2008).
14. Burch, D., Singh, G., Ceder, G. & Bazant, M. Z. Phase-transformation wave dynamics in LiFePO4. *Solid State Phenom.* **139**, 95–100 (2008).
15. Nadkarni, N. *et al.* Interplay of phase boundary anisotropy and electro-auto-catalytic surface reactions on the lithium intercalation dynamics in LiXFePO4 plateletlike nanoparticles. *Phys. Rev. Mater.* **2**, 1–13 (2018).
16. Tang, M., Belak, J. F. & Dorr, M. R. Anisotropic phase boundary morphology in nanoscale olivine electrode particles. *J. Phys. Chem. C* **115**, 4922–4926 (2011).
17. Delmas, C., Maccario, M., Croguennec, L., Le Cras, F. & Weill, F. Lithium deintercalation in LiFePO4 nanoparticles via a domino-cascade model. *Nat. Mater.* **7**, 665–671 (2008).
18. Lim, J. *et al.* Origin and hysteresis of lithium compositional spatiodynamics within battery primary particles. *Science* **353**, 566–571 (2016).
19. Liu, H. *et al.* Capturing metastable structures during high-rate cycling of LiFePO 4 nanoparticle electrodes. *Science* **344**, (2014).
20. Bazant, M. Z. Thermodynamic stability of driven open systems and control of phase separation by electro-autocatalysis. *Faraday Discuss.* **199**, 423–463 (2017).
21. Bai, P., Cogswell, D. A. & Bazant, M. Z. Suppression of phase separation in LiFePO4 nanoparticles during battery discharge. *Nano Lett.* **11**, 4890–4896 (2011).
22. Cogswell, D. A. & Bazant, M. Z. Theory of coherent nucleation in phase-separating nanoparticles. *Nano Lett.* **13**, 3036–3041 (2013).
23. Cogswell, D. A. & Bazant, M. Z. Size-dependent phase morphologies in LiFePO4 battery particles. *Electrochem. commun.* **95**, 33–37 (2018).
24. Welland, M. J., Karpeyev, D., O'Connor, D. T. & Heinonen, O. Miscibility Gap Closure, Interface Morphology, and Phase Microstructure of 3D LixFePO4 Nanoparticles from Surface Wetting and Coherency Strain. *ACS Nano* **9**, 9757–9771 (2015).
25. Dreyer, W. *et al.* The thermodynamic origin of hysteresis in insertion batteries.

Nat. Mater. **9**, 448–453 (2010).

26. Ferguson, T. R. & Bazant, M. Z. Phase transformation dynamics in porous battery electrodes. *Electrochim. Acta* **146**, 89–97 (2014).
27. Li, Y. *et al.* Current-induced transition from particle-by-particle to concurrent intercalation in phase-separating battery electrodes. *Nat. Mater.* **13**, 1149–1156 (2014).
28. Malik, R., Burch, D., Bazant, M. & Ceder, G. Particle size dependence of the ionic diffusivity. *Nano Lett.* **10**, 4123–4127 (2010).
29. Nishimura, S. I. *et al.* Experimental visualization of lithium diffusion in LixFePO 4. *Nat. Mater.* **7**, 707–711 (2008).
30. Morgan, D., Van der Ven, A. & Ceder, G. Li Conductivity in LixMPO4 (M = Mn, Fe, Co, Ni) Olivine Materials. *Electrochem. Solid-State Lett.* **7**, 2003–2005 (2004).
31. Hong, L. *et al.* Two-dimensional lithium diffusion behavior and probable hybrid phase transformation kinetics in olivine lithium iron phosphate. *Nat. Commun.* **8**, (2017).
32. Mefford, J. T. *et al.* Correlative operando microscopy of oxygen evolution electrocatalysts. *Nature* **593**, (2021).
33. Ohmer, N. *et al.* Phase evolution in single-crystalline LiFePO4 followed by in situ scanning X-ray microscopy of a micrometre-sized battery. *Nat. Commun.* **6**, 1–7 (2015).
34. De Smit, E. *et al.* Nanoscale chemical imaging of a working catalyst by scanning transmission X-ray microscopy. *Nature* **456**, 222–225 (2008).
35. Li, Z. *et al.* [100]-Oriented LiFePO4 Nanoflakes toward High Rate Li-Ion Battery Cathode. *Nano Lett.* **16**, 795–799 (2016).
36. Li, Z. *et al.* Orientation-Dependent Lithium Miscibility Gap in LiFePO4. *Chem. Mater.* **30**, 874–878 (2018).
37. Zhu, Y. *et al.* In situ atomic-scale imaging of phase boundary migration in FePO 4 microparticles during electrochemical lithiation. *Adv. Mater.* **25**, 5461–5466 (2013).
38. Chueh, W. C. *et al.* Intercalation pathway in many-particle LiFePO4 electrode revealed by nanoscale state-of-charge mapping. *Nano Lett.* **13**, 866–872 (2013).

39. Dou, J. *et al.* Photochemical degradation of iron(III) citrate/citric acid aerosol quantified with the combination of three complementary experimental techniques and a kinetic process model. *Atmos. Chem. Phys.* **21**, 315–338 (2021).
40. Shapiro, D. A. *et al.* Chemical composition mapping with nanometre resolution by soft X-ray microscopy. *Nat. Photonics* **8**, 765–769 (2014).
41. Zhang, X. *et al.* Direct view on the phase evolution in individual LiFePO 4 nanoparticles during Li-ion battery cycling. *Nat. Commun.* **6**, 1–7 (2015).
42. Hess, M., Sasaki, T., Villevieille, C. & Novák, P. Combined operando X-ray diffraction-electrochemical impedance spectroscopy detecting solid solution reactions of LiFePO4 in batteries. *Nat. Commun.* **6**, 1–9 (2015).
43. Bai, P. & Bazant, M. Z. Charge transfer kinetics at the solid-solid interface in porous electrodes. *Nat. Commun.* **5**, (2014).
44. Park, J. *et al.* Fictitious phase separation in Li layered oxides driven by electro-autocatalysis. *Nat. Mater.* (2021).
45. Zhao, H. & Bazant, M. Z. Population dynamics of driven autocatalytic reactive mixtures. *Phys. Rev. E* **100**, 1–11 (2019).
46. Cogswell, D. A. & Bazant, M. Z. Coherency strain and the kinetics of phase separation in LiFePO 4 nanoparticles. *ACS Nano* **6**, 2215–2225 (2012).
47. Fraggedakis, D. *et al.* Theory of coupled ion-electron transfer kinetics. *Electrochim. Acta* **367**, 137432 (2020).
48. Park, J. *et al.* Fictitious phase separation in Li layered oxides driven by electro-autocatalysis. *Nat. Mater.* **20**, 991–999 (2021).
49. Hong, L., Yang, K. & Tang, M. A mechanism of defect-enhanced phase transformation kinetics in lithium iron phosphate olivine. *npj Comput. Mater.* **5**, 1–9 (2019).
50. Dathar, G. K. P., Sheppard, D., Stevenson, K. J. & Henkelman, G. Calculations of Li-ion diffusion in olivine phosphates. *Chem. Mater.* **23**, 4032–4037 (2011).
51. Bazant, M. Z. Theory of chemical kinetics and charge transfer based on nonequilibrium thermodynamics. *Acc. Chem. Res.* **46**, 1144–1160 (2013).
52. Kang, B. & Ceder, G. Battery materials for ultrafast charging and discharging. *Nature* **458**, 190–193 (2009).
53. Pan, R., Rau, D., Moryson, Y., Sann, J. & Janek, J. Reversible Capacity Loss of

LiCoO2Thin Film Electrodes. *ACS Appl. Energy Mater.* **3**, 6065–6071 (2020).

54. Wu, S.-L. *et al.* High Rate Capability of Li(Ni 1/3 Mn 1/3 Co 1/3)O 2 Electrode for Li-Ion Batteries . *J. Electrochem. Soc.* **159**, A438–A444 (2012).
55. Gowda, S. R., Dees, D. W., Jansen, A. N. & Gallagher, K. G. Examining the Electrochemical Impedance at Low States of Charge in Lithium- and Manganese-Rich Layered Transition-Metal Oxide Electrodes. *J. Electrochem. Soc.* **162**, A1374–A1381 (2015).
56. Gonzalez-Rosillo, J. C. *et al.* Lithium-Battery Anode Gains Additional Functionality for Neuromorphic Computing through Metal–Insulator Phase Separation. *Adv. Mater.* **32**, 1907465 (2020).
57. Fuller, E. J. *et al.* Li-Ion Synaptic Transistor for Low Power Analog Computing. *Adv. Mater.* **29**, 1604310 (2017).
58. Tian, H. & Bazant, M. Z. Interfacial Resistive Switching by Multiphase Polarization in Ion-Intercalation Nanofilms. *Nano Lett.* **22**, 5866–5873 (2022).
59. Nadkarni, N., Zhou, T., Fraggedakis, D., Gao, T. & Bazant, M. Z. Modeling the Metal–Insulator Phase Transition in LixCoO2 for Energy and Information Storage. *Adv. Funct. Mater.* **29**, 1–9 (2019).